

**Thermal dilepton rate and electrical conductivity:
An analysis of vector current correlation functions in
quenched lattice QCD**

H.-T. Ding^{1,2}, A. Francis¹, O. Kaczmarek¹, F. Karsch^{1,2},
E. Laermann¹ and W. Soeldner¹

¹ Fakultät für Physik, Universität Bielefeld, D-33615 Bielefeld, Germany

² Physics Department, Brookhaven National Laboratory, Upton, NY 11973, USA

ABSTRACT

We calculate the vector current correlation function for light valence quarks in the deconfined phase of QCD. The calculations have been performed in quenched lattice QCD at $T \simeq 1.45T_c$ for four values of the lattice cut-off on lattices up to size $128^3 \times 48$. This allows to perform a continuum extrapolation of the correlation function in the Euclidean time interval $0.2 \leq \tau T \leq 0.5$, which extends to the largest temporal separations possible at finite temperature, to better than 1% accuracy. In this interval, at the value of the temperature investigated, we find that the vector correlation function never deviates from the free correlator for massless quarks by more than 9%. We also determine the first two non-vanishing thermal moments of the vector meson spectral function. The second thermal moment deviates by less than 7% from the free value. With these constraints, we then proceed to extract information on the spectral representation of the vector correlator and discuss resulting consequences for the electrical conductivity and the thermal dilepton rate in the plasma phase.

I. INTRODUCTION

Many of the properties of deconfined, strongly interacting matter are reflected in the structure of correlation functions of the vector current. Its spectral representation directly relates to the invariant mass spectrum of dileptons and photons. Depending on the invariant mass regime one can get information on in-medium properties of heavy [1] and light [2] quark bound states. For low invariant masses one enters the hydrodynamic regime where spectral functions reflect transport properties of the thermal medium [3–8]. In the case of the vector correlation function and its spectral representation this is characterized by a transport coefficient, the electrical conductivity. Heavy ion experiments start getting sensitive to the relevant regime of low mass dileptons/photons of a few hundred MeV, *i.e.* invariant masses that are of the order of the scale set by the QCD transition temperature [9].

Spectral functions in the vector channel, or equivalently cross sections for thermal dilepton production have been extensively studied in perturbation theory [10, 11]. Non-perturbative aspects have been included through the hard thermal loop resummation scheme [12]. A straightforward application of the latter, however, breaks down in the low invariant mass regime. This finds its manifestation in a too rapid rise of the spectral density which, in turn, leads to an infrared divergent Euclidean correlator of the vector current [13]. This low invariant mass regime has been examined in much detail [14, 15] and it has been demonstrated that the spectral function at low energies will increase linearly with energy giving rise to a finite, non vanishing electrical conductivity of the quark gluon plasma.

Lattice calculations of Euclidean time correlation functions can give access to spectral functions [16]. Extracting these directly, however, is an ill-posed problem and progress in this direction has been made only recently through the application of statistical tools like the Maximum Entropy Method (MEM) [17]. Subsequently this method has been applied to also analyze correlation functions of the vector current [18–20].

In this paper we analyze the behavior of the vector correlation function at high temperature, *i.e.* in the deconfined phase of QCD. Our first goal is to generate precise data for this correlator which allow for its extrapolation to the continuum limit in a time interval extending to the largest temporal separations possible at finite T . From the large τ behavior of the correlator we then collect evidence for non-perturbative structure of the corresponding spectral function at low energy. This forms the basis for the extraction of information on the spectral representation of the vector correlator by starting with an ansatz for the spectral function as well as by exploiting the Maximum Entropy Method (MEM).

The paper is organized as follows. In the next section we collect basic formulas for vector correlation functions and their spectral representation which are related to the thermal dilepton rate as well as the electrical conductivity. Section III introduces thermal moments of vector correlation functions. In Section IV we present our numerical results on the vector correlation function calculated at $T \simeq 1.45T_c$. In Section V we discuss an analysis of these results based on fits to the data as well as on an analysis using the MEM. In Section VI we discuss consequences for the calculation of dilepton and photon rates as well as the electrical conductivity. We finally give our conclusions and an outlook on future studies in Section VII.

II. THERMAL VECTOR CORRELATION FUNCTION, DILEPTON RATE AND ELECTRICAL CONDUCTIVITY

A. Correlation functions

Let us start by summarizing some basic relations between the Euclidean correlation function of the vector current,

$$J_\mu(\tau, \vec{x}) \equiv \bar{q}(\tau, \vec{x}) \gamma_\mu q(\tau, \vec{x}) , \quad (\text{II.1})$$

at non-zero temperature and its spectral representation on the one hand and thermal dilepton rates and the electrical conductivity on the other hand.

We will analyze Euclidean time two-point functions of the current J_μ at fixed momentum,

$$G_{\mu\nu}(\tau, \vec{p}) = \int d^3x G_{\mu\nu}(\tau, \vec{x}) e^{i\vec{p}\cdot\vec{x}} , \quad (\text{II.2})$$

with

$$G_{\mu\nu}(\tau, \vec{x}) = \langle J_\mu(\tau, \vec{x}) J_\nu^\dagger(0, \vec{0}) \rangle . \quad (\text{II.3})$$

Here $\langle \dots \rangle$ denotes thermal expectation values.

The vector current receives contributions from connected as well as disconnected diagrams. However, contributions from the latter are parametrically small. In high temperature perturbation theory they occur at $\mathcal{O}(g^6 \ln 1/g)$ and give rise to the difference between quark number and isospin susceptibilities [21]. This difference has been found to be small at all temperatures in the high temperature phase of QCD [22, 23]. Moreover, in calculations of the correlation function of the electromagnetic current,

$$J_{em} = \sum_f Q_f \bar{q}^f(\tau, \vec{x}) \gamma_\mu q^f(\tau, \vec{x}) , \quad (\text{II.4})$$

the contribution of disconnected diagrams vanishes for three degenerate quark flavors as it is proportional to the square of the sum of elementary charges Q_f . The connected part, on the other hand is proportional to the sum of the square of the elementary charges of the quark flavor f , $C_{em} = \sum_f Q_f^2$. In the following we will limit our discussion to the connected part of the vector current, as it is generally done in the analysis of thermal observables deduced from the electromagnetic current.

The current-current correlation functions can be represented in terms of an integral over spectral functions, $\rho_{\mu\nu}(\omega, \vec{p}, T)$, which are odd functions of the 4-momentum, *i.e.* $\rho_{\mu\nu}(\omega, \vec{p}, T) = -\rho_{\mu\nu}(-\omega, -\vec{p}, T)$. We denote by ρ_{ii} the sum over the three space-space components of the spectral function and also introduce the vector spectral function $\rho_V \equiv \rho_{00} + \rho_{ii}$. With this we obtain the corresponding correlation functions,

$$G_H(\tau, \vec{p}, T) = \int_0^\infty \frac{d\omega}{2\pi} \rho_H(\omega, \vec{p}, T) \frac{\cosh(\omega(\tau - 1/2T))}{\sinh(\omega/2T)} , \quad H = 00, ii, V . \quad (\text{II.5})$$

In the following we will limit ourselves to an analysis of Euclidean time correlation functions at vanishing three-momentum. Therefore we will drop the second argument of the correlation and

spectral functions and also suppress the argument for the explicit temperature dependence, e.g. $G_H(\tau T) \equiv G_H(\tau, \vec{0}, T)$. Occasionally we also find it convenient to express dimensionful quantities in appropriate units of temperature. For this purpose we will introduce dimensionless variables, e.g. $\tilde{\omega} = \omega/T$, $\tilde{\tau} = \tau T$ and $\tilde{G}_H = G_H/T^3$.

B. Spectral functions

The integral over the 0^{th} component of the vector current is the net number of quarks ($q-\bar{q}$) in a given flavor channel, $n_0(\tau) = \int d^3x J_0(\tau, \vec{x})$. As the net number of quarks is conserved, it also does not depend on Euclidean time τ , *i.e.* $n_0(\tau) = n_0(0)$. Consequently the corresponding correlation function, $G_{00}(\tau T)$, is constant in Euclidean time and its spectral representation is simply given by a δ -function,

$$\rho_{00}(\omega) = -2\pi\chi_q\omega\delta(\omega) , \quad (\text{II.6})$$

where χ_q is the quark number susceptibility^a

$$\chi_q = -\frac{1}{T} \int d^3x \langle J_0(\tau, \vec{x}) J_0^\dagger(0, \vec{0}) \rangle . \quad (\text{II.7})$$

The time-time component of the correlation function thus is proportional to the quark number susceptibility, $G_{00}(\tau T) = -\chi_q T$. The vector correlation functions G_{ii} and G_V therefore differ only by a constant,

$$G_{ii}(\tau T) = \chi_q T + G_V(\tau T) . \quad (\text{II.8})$$

The spatial components of the vector spectral function, $\rho_{ii}(\omega)$, increase quadratically for large values of ω . In the free field limit one obtains for massless quarks,

$$\begin{aligned} \rho_{00}^{\text{free}}(\omega) &= -2\pi T^2 \omega \delta(\omega) , \\ \rho_{ii}^{\text{free}}(\omega) &= 2\pi T^2 \omega \delta(\omega) + \frac{3}{2\pi} \omega^2 \tanh(\omega/4T) . \end{aligned} \quad (\text{II.9})$$

Note that in this limit the contributions of δ -functions in ρ_{00} and ρ_{ii} cancel in the vector spectral function $\rho_V(\omega) \equiv \rho_{00}(\omega) + \rho_{ii}(\omega)$. This is no longer the case in an interacting theory at finite temperature.

At high temperature and for large energies corrections to the free field behavior can be calculated perturbatively; the vector spectral function can be deduced from the calculation of one loop corrections to the leading order results for the thermal dilepton rate [24]. This yields,

$$\rho_{ii}(\omega) \simeq \frac{3}{2\pi} \left(1 + \frac{\alpha_s}{\pi}\right) \omega^2 \tanh(\omega/4T) \quad , \quad \omega/T \gg 1 . \quad (\text{II.10})$$

At energies $\omega \lesssim T$ perturbative calculations as well as the resummation of certain subsets of diagrams (hard thermal loop (HTL) resummation [12]) become complicated as several scales of order $g^n T$ start becoming important. In fact, the straightforward HTL-resummation [12] is known to lead

^a As discussed above we only consider the connected part of the vector correlation functions. Within this approximation χ_q is actually not the quark number susceptibility but the isospin susceptibility [23].

to a infrared divergent spectral function, $\rho_{\text{HTL}}(\omega) \sim 1/\omega$, which also leads to a divergent vector correlation function [13].

The limit $\omega \rightarrow 0$ is sensitive to transport properties in the thermal medium and the spectral functions need to be linear in ω in order to give rise to a non-vanishing, finite transport coefficient; in this limit the spatial components of the vector spectral function yield the electrical conductivity

$$\frac{\sigma}{T} = \frac{C_{em}}{6} \lim_{\omega \rightarrow 0} \frac{\rho_{ii}(\omega)}{\omega T}. \quad (\text{II.11})$$

In the free field, infinite temperature limit also the spatial part of the spectral function contains a δ -function at the origin. Different from the time-time component, where the δ -function is protected by current conservation, this δ -function is smeared out at finite temperature and the low energy part of ρ_{ii} is expected to be well described by a Breit-Wigner peak [3–5, 7, 8],

$$\rho_{ii}^{BW}(\omega) = \chi_q c_{BW} \frac{\omega \Gamma}{\omega^2 + (\Gamma/2)^2}, \quad (\text{II.12})$$

which yields $\sigma(T)/C_{em} = 2\chi_q c_{BW}/(3\Gamma)$. In the infinite temperature limit the width of the Breit-Wigner peak vanishes; at the same time $c_{BW} \rightarrow 1$, $\chi_q \rightarrow T^2$ and consequently the electrical conductivity is infinite in the non-interacting case.

In the high temperature regime the time-time component of the spectral function receives perturbative corrections, reflecting the perturbative corrections to the quark number susceptibility. To leading order this gives

$$\rho_{00} = -2\pi T^2 \omega \delta(\omega) \left(1 - \frac{1}{2\pi^2} g^2(T) \right). \quad (\text{II.13})$$

C. Thermal dilepton and photon rates

The vector spectral function is directly related to the thermal production rate of dilepton pairs with squared invariant mass $\omega^2 - \vec{p}^2$,

$$\frac{dN_{l+l-}}{d\omega d^3p} = C_{em} \frac{\alpha_{em}^2}{6\pi^3} \frac{\rho_V(\omega, \vec{p}, T)}{(\omega^2 - \vec{p}^2)(e^{\omega/T} - 1)}, \quad (\text{II.14})$$

where α_{em} is the electromagnetic fine structure constant.

The vector spectral function at light-like 4-momentum yields the photon emission rate of a thermal medium,

$$\omega \frac{dR_\gamma}{d^3p} = C_{em} \frac{\alpha_{em}}{4\pi^2} \frac{\rho_V(\omega = |\vec{p}|, T)}{e^{\omega/T} - 1}. \quad (\text{II.15})$$

The emission rate of soft photons, thus can be related to the electrical conductivity,

$$\lim_{\omega \rightarrow 0} \omega \frac{dR_\gamma}{d^3p} = \frac{3}{2\pi^2} \sigma(T) T \alpha_{em}. \quad (\text{II.16})$$

III. MOMENTS OF THE VECTOR SPECTRAL FUNCTION

In addition to the vector correlation function itself we will calculate its curvature at the largest Euclidean time separation accessible at non-zero temperature, *i.e.* at $\tau T = 1/2$. The curvature is

the second *thermal moment* of the spectral functions at vanishing momentum,

$$G_H^{(n)} = \frac{1}{n!} \left. \frac{d^n G_H(\tau T)}{d(\tau T)^n} \right|_{\tau T=1/2} = \frac{1}{n!} \int_0^\infty \frac{d\omega}{2\pi} \left(\frac{\omega}{T} \right)^n \frac{\rho_H(\omega)}{\sinh(\omega/2T)} , \quad H = ii, V , \quad (\text{III.1})$$

where n is chosen to be even as all odd moments vanish. These thermal moments give the Taylor expansion coefficients for the correlation function expanded around the mid-point of the Euclidean time interval, *i.e.* around $\tau T = 1/2$,

$$G_H(\tau T) = \sum_{n=0}^{\infty} G_H^{(2n)} \left(\frac{1}{2} - \tau T \right)^{2n} . \quad (\text{III.2})$$

It is obvious from Eq. III.1 that in a calculation of the n -th moment the spectral function is weighted by a term, which has a pronounced maximum at $\tanh(\omega/2T) = \omega/2nT$. The n -th order moment thus is most sensitive to the spectral function at $\omega/T \simeq 2n$ and we may expect that higher order moments will come close to results obtained with perturbative spectral functions.

In the infinite temperature, free field limit the integral in Eq. II.5 can be evaluated analytically and one obtains for massless quarks [25],

$$\begin{aligned} G_V^{free}(\tau T) &= 6T^3 \left(\pi (1 - 2\tau T) \frac{1 + \cos^2(2\pi\tau T)}{\sin^3(2\pi\tau T)} + 2 \frac{\cos(2\pi\tau T)}{\sin^2(2\pi\tau T)} \right) , \\ G_{ii}^{free}(\tau T) &= T^3 + G_V^{free}(\tau T) . \end{aligned} \quad (\text{III.3})$$

From this we easily obtain the moments of the free spectral functions. The first three non-vanishing moments are given by

$$G_V^{(0),free} = \frac{2}{3} G_{ii}^{(0),free} = 2T^3 , \quad G_H^{(2),free} = \frac{28\pi^2}{5} T^3 , \quad G_H^{(4),free} = \frac{124\pi^4}{21} T^3 . \quad (\text{III.4})$$

We note that $G_{ii}^{(n)} = G_V^{(n)}$ for all $n > 0$ not only at an infinite but at all values of the temperature as the correlators G_{ii} and G_V only differ by a constant (Eq. II.8). However, while in the free field limit $G_{ii}(\tau T)$ contains a constant contribution which drops out in the calculation of higher moments ($n > 0$), this is no longer the case at finite values of the temperature: all thermal moments, $G_H^{(2n)}$ with $n \geq 0$, will be sensitive to the smeared δ -function contributing to $\rho_{ii}(\omega)$ although, as indicated above, we expect this contribution to become more and more suppressed in higher order moments.

In the following we will analyze the ratio of $G_H(\tau T)$ and the free field correlator $G_H^{free}(\tau T)$,

$$\frac{G_H(\tau T)}{G_H^{free}(\tau T)} = \frac{G_H^{(0)}}{G_H^{(0),free}} \left(1 + \left(R_H^{(2,0)} - R_{H,free}^{(2,0)} \right) \left(\frac{1}{2} - \tau T \right)^2 + \dots \right) , \quad (\text{III.5})$$

as well as the ratio of mid-point subtracted correlation functions

$$\begin{aligned} \Delta_V(\tau T) &\equiv \frac{G_V(\tau T) - G_V^{(0)}}{G_V^{free}(\tau T) - G_V^{(0),free}} \\ &= \frac{G_V^{(2)}}{G_V^{(2),free}} \left(1 + \left(R_V^{(4,2)} - R_{V,free}^{(4,2)} \right) \left(\frac{1}{2} - \tau T \right)^2 + \dots \right) . \end{aligned} \quad (\text{III.6})$$

Here we used the notation $R_H^{(n,m)} \equiv G_H^{(n)}/G_H^{(m)}$. Note that the curvature of these ratios at the mid-point determines the deviation of ratios of thermal moments from the corresponding free field values. While the ratios of correlation functions differ in the $H = ii$ and $H = V$ channels due to the additional constant contributing to $G_V(\tau T)$, this constant drops out in the subtracted correlation function, *i.e.*, $\Delta_V(\tau T) \equiv \Delta_{ii}(\tau T)$ and $G_V^{(n)} = G_{ii}^{(n)}$ for $n > 0$.

N_τ	β	T/T_c	c_{SW}	κ	Z_V
16	6.872	1.46	1.4125	0.13495	0.829
24 (I)	7.192	1.42	1.3673	0.13431	0.842
24 (II)				0.13440	
32	7.457	1.45	1.3389	0.13390	0.851
48	7.793	1.43	1.3104	0.13340	0.861

TABLE I. Simulation parameters for the generation of gauge field configurations on lattices of size $N_\sigma^3 \times N_\tau$.

β	κ	$m_{AWI}/T[\mu = 1/a]$	$m_{\overline{MS}}/T[\mu = 2GeV]$	$m_{\overline{MS}}[\mu = 2GeV]$ [MeV]
6.872	0.13495	0.0182(4)	0.0243(1)	9.5
7.192	0.13440	0.0182(4)	0.0237(1)	9.3
7.192	0.13431	0.0816(2)	0.1062(2)	41.6
7.457	0.13390	0.0790(3)	0.0989(4)	38.7
7.793	0.13340	0.0964(2)	0.1117(2)	43.7

TABLE II. AWI and \overline{MS} quark masses in units of the temperature. For orientation we show in the last column estimates for the quark masses in units of MeV. These values have been obtained using for the phase transition temperature in the SU(3) gauge theory $T_c \simeq 270$ MeV.

IV. COMPUTATIONAL DETAILS AND NUMERICAL RESULTS

All our numerical results are obtained from an analysis of quenched QCD gauge field configurations generated with the standard SU(3) single plaquette Wilson gauge action [26]. On these gauge field configurations correlation functions have been calculated using a clover action with non-perturbatively determined clover coefficients c_{SW} and a hopping parameter κ chosen close to its critical value [27, 28].

The gauge couplings used for calculations at four different values of the cut-off ($aT = 1/N_\tau$) have been selected such that the temperature stays approximately constant as the cut-off is varied; $T \simeq 1.45T_c$. For this we used an ansatz originally suggested in Ref. [29]. It is known to give the variation of the lattice cut-off as function of the gauge coupling to better than 1% in the interval [5.6, 6.5] [30]. We added to this analysis new results for the critical coupling $\beta_c(N_\tau)$ and the square root of the string tension $\sqrt{\sigma}$ [31] and extrapolated the fit results to the regime of couplings relevant for our analysis, *i.e.* $\beta \in [6.8, 7.8]$.

By tuning the Wilson hopping parameter κ in the fermion action we have chosen quark masses that are approximately constant for our four values of the cut-off. We have estimated the quark masses using the axial Ward identity (AWI) to calculate the so called AWI current quark mass, m_{AWI} , for the different values of the cut-off [32]. Here we used a non-perturbatively improved axial-vector current with coefficient c_A from [27, 33].

To compare the quark masses at a common scale we first converted to renormalization group invariant quark masses [34] using non-perturbative coefficients [35, 36] and then rescaled in the \overline{MS} scheme to the common scale $\mu = 2$ GeV using the four-loop perturbative running from [37]. In

N_τ	N_σ	β	# conf
16	32	6.872	251
	48	6.872	229
	64	6.872	191
	128	6.872	191
24 (I)	128	7.192	340
24 (II)	128	7.192	156
32	128	7.457	255
48	128	7.793	451

TABLE III. Number of configurations analyzed on lattices of size $N_\sigma^3 \times N_\tau$. All configurations are separated by 500 Monte Carlo iterations.

both cases errors are calculated from a jackknife analysis on m_{AWI} and do not include systematic errors for the conversion to the \overline{MS} scheme.

All basic parameters that enter our simulations are summarized in Table I. The values for the quark masses used in our calculations are quoted in Table II. Our central results are based on calculations performed with renormalized quark masses $m_{\overline{MS}}/T \simeq 0.1$. Through calculations performed with a factor 4 smaller quark mass we checked on lattices with temporal extent $N_\tau = 24$ that results on the large distance behavior of correlation functions agree within errors (see Fig. 1). This smaller quark mass has also been used for the calculations on our coarsest lattice corresponding to a temporal lattice size $N_\tau = 16$, where we analyzed the sensitivity of our results to finite volume effects. We thus expect that quark mass effects play no role in all results presented here.

We have generated the gauge field configurations by using an over-relaxed heat bath algorithm. Configurations have been stored after every 500 sweeps. We have checked at several large temporal separations that the correlation functions calculated on these configurations are statistically independent. We further have measured the plaquette every sweep to obtain an estimate for the integrated autocorrelation time of order 1. Note that at temperatures above deconfinement topologically non-trivial configurations die out quickly. This is reflected in the observation that the inspection of the scalar and pseudo-scalar correlator revealed less than 3 % so-called exceptional configurations^b which had an autocorrelation time of 3000 sweeps at most. The statistics accumulated on different size lattices is collected in Table III.

For the computation of the quark propagators we used a plain conjugate gradient inverter. The algorithm has a stable convergence behavior, however, we found it appropriate to set the convergence criterion to 10^{-23} for the squared norm of the residue. This value was selected by monitoring the nearly exponential decay of spatial correlation functions which range over many orders of magnitude due to the large spatial extent of the lattices and screening masses of the order of $2\pi T$.

For the calculation of the time-time (G_{00}) and space-space (G_{ii}) components of the vector correlation function we use the local vector current $J_\mu(\tau, \vec{x})$ introduced in Eq. II.1. Unlike point-

^b Note that zero modes do not couple into the vector and axial vector correlation functions.

split vector currents, this local lattice current is not conserved at non-zero lattice spacing. As a consequence the time-time component $G_{00}(\tau T)$ may not strictly be τ -independent at finite values of the cut-off [39]. Furthermore, the current needs to be renormalized multiplicatively. Wherever required we therefore use the renormalized vector current,

$$J_\mu^{lat}(\tau, \vec{x}) = (2\kappa Z_V) \bar{q}(\tau, \vec{x}) \gamma_\mu q(\tau, \vec{x}) , \quad (\text{IV.1})$$

with Z_V denoting the non-perturbatively determined renormalization constant [28] also given in Table I.

However, we note that many results presented in the following are given in terms of ratios of correlation functions as well as mid-point subtracted correlation functions divided by the quark number susceptibility, $\tilde{\chi}_q \equiv \chi_q/T^2$. These ratios are independent of any multiplicative renormalization.

It is obvious from Eq. III.5 that the correlators $G_V(\tau T)$ and $G_{ii}(\tau T)$ are identical up to a constant, $G_{00}(\tau T) \equiv \chi_q T^2$. It thus suffices to analyze one of them. In the following we will mainly concentrate on a discussion of $G_V(\tau T)$. This is because a subtle cancellation occurs between the constant contribution $\chi_q T^2$ to $G_V(\tau T)$ and the Breit-Wigner term in the spatial part ($G_{ii}(\tau T)$). In the free field limit this cancellation is exact. It is the incomplete cancellation of these two contributions to $G_V(\tau T)$ which gives rise to the weak dependence of G_V/G_V^{free} on Euclidean time and contains information on transport coefficients. Of course, the constant contribution $\chi_q T^2$ is trivial when it comes to an analysis of the spectral representation of vector correlation functions. For the determination of the spectral function $\rho_{ii}(\omega)$ the correlator $G_{ii}(\tau T)$ thus is much more relevant. For this reason we will also show some results on the spatial correlator.

A. Correlation functions of the vector current

The vector current correlation function was calculated previously, using the same non-perturbatively improved clover action, on lattices of size $64^3 \times 16$ [18]. A MEM analysis was used to determine thermal dilepton rates which suggested a suppression of the spectral weight relative to the free spectral function at small energies. Subsequently vector correlation functions at high temperature were analyzed using staggered fermion formulations [19, 20] and a modified kernel was used in the MEM analysis [20]. This modification of the MEM algorithm increased the sensitivity of MEM to the low energy structure of spectral functions and resolved part of the problems observed in [18]. We will show below that it is also crucial in a MEM analysis to choose default models which allow for a linear slope of the spectral functions at small energies.

Calculations of vector spectral functions using staggered fermions are more involved, as two spectral functions, corresponding to different parity channels, need to be determined simultaneously. These studies were performed using lattices with temporal extent up to $N_\tau = 14$ [19] and $N_\tau = 24$ [20], respectively. They were performed with unrenormalized currents and primarily aimed at a determination of the (unrenormalized) electrical conductivity. They led, however, to quite different results, $\sigma/T \simeq 7C_{em}$ [19] and $\sigma/T \simeq (0.4 \pm 0.1)C_{em}$ [20].

Here we improve over these studies with staggered fermions as well as the analysis of the thermal dilepton rate performed with improved Wilson fermions [18] by using the latter approach and doubling the spatial lattice extent to $N_\sigma = 128$ as well as increasing the temporal lattice extent by

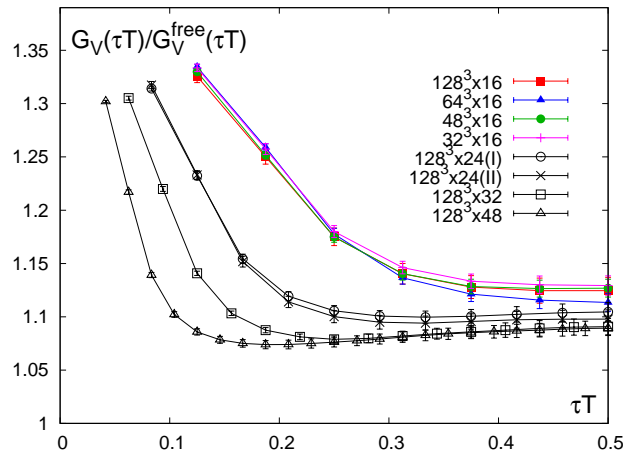


FIG. 1. The vector correlation function, $G_V(\tau T)$, calculated on lattices of size $N_\sigma^3 \times N_\tau$ at $T \simeq 1.45T_c$. The correlation functions are normalized to the free vector correlation function $G_V^{free}(\tau T)$ in the continuum. Shown are data for $\tau T > 1/N_\tau$ only. Label I and II refer to data sets generated with two different values of the quark mass (see Table I).

up to a factor three. We have calculated the vector correlation function on lattices of size $N_\sigma^3 \times N_\tau$, with $32 \leq N_\sigma \leq 128$ and $N_\tau = 16, 24, 32$ and 48 . For $N_\tau = 16$ we have calculated $G_H(\tau T)$ on lattices with spatial extent $N_\sigma = 32, 64, 96$ and 128 . For $N_\tau = 24$ we checked that the quark masses used in our calculations are indeed small enough on the scale of the temperature to be ignored in the analysis of our correlation functions. On the largest spatial lattice, $N_\sigma = 128$, we performed calculations for four different values of the lattice cut-off by choosing $N_\tau = 16, 24, 32$ and 48 and at the same time changing the value of the gauge coupling β such that the temperature is kept constant, $T \simeq 1.45T_c$.

The large range of spatial lattice sizes used in this calculation, $2 \leq N_\sigma/N_\tau \leq 8$, allows to quantify finite volume effects at fixed values of the lattice cut-off, $aT = 1/N_\tau$. The large temporal lattice allows to reduce the lattice spacing at $T \simeq 1.45T_c$ to about 0.01 fm. Its variation by a factor three gives us good control over lattice cut-off effects. As will become clear in the following, finite volume effects are well under control and the variation of the lattice cut-off by a factor three now allows for the extrapolation to the continuum limit. This removes systematic errors that were present in earlier calculations performed with the same discretization scheme used here [18].

As the dependence of $G_H(\tau T)$ on Euclidean time τ is very similar to that of the free vector correlation function, we eliminate the dominant exponential variation of $G_H(\tau T)$ with τT and show in Fig. 1 the ratio $G_V(\tau T)/G_V^{free}(\tau T)$ introduced in Eq. III.5 for all parameter sets analyzed by us. We note that finite volume effects increase somewhat with τT , but remain small even for the largest Euclidean time separation $\tau T = 1/2$. Cut-off effects show the opposite trend; they increase with decreasing τT . In fact, they strongly influence the behavior of $G_V(\tau T)$ at short distances for the first 6 to 8 Euclidean time units, $1/N_\tau \leq \tau T \lesssim 8/N_\tau$. It also is obvious from Fig. 1 that deviations from the free field correlation function change qualitatively when the lattice spacing is reduced. For $N_\tau \geq 24$ the ratio $G_V(\tau T)/G_V^{free}(\tau T)$ increases close to $\tau T = 1/2$ indicating that the ratio of thermal moments, $R_V^{(2,0)}$, is smaller than the corresponding free field

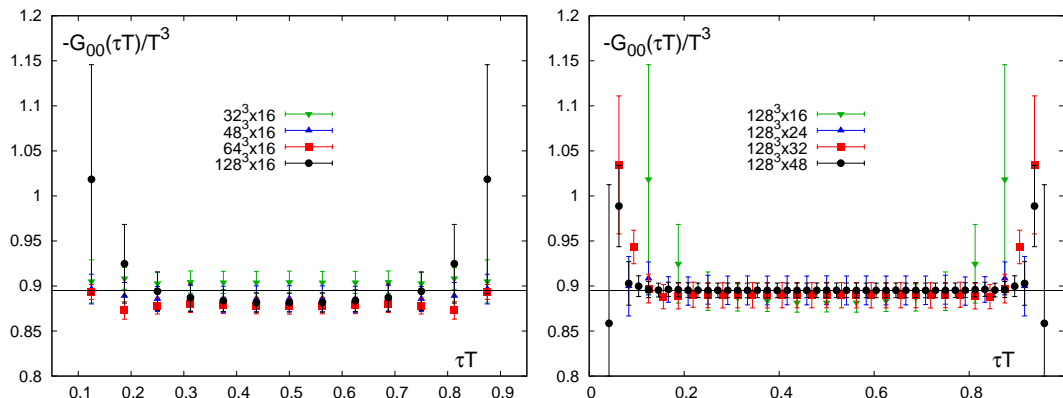


FIG. 2. The time-time component of the vector correlation function, $G_{00}(\tau T)/T^3$, calculated at $T \simeq 1.45T_c$ versus Euclidean time τT . The left hand part of the figure shows the volume dependence of $G_{00}(\tau T)/T^3$ for $N_\tau = 16$ and $32 \leq N_\sigma \leq 128$. The right hand figure shows the cut-off dependence of $G_{00}(\tau, T)/T^3$ for $N_\sigma = 128$ and $16 \leq N_\tau \leq 48$. In both figures the horizontal line shows a fit to the data obtained on the largest lattice, $128^3 \times 48$.

N_τ	16	24	32	48	∞
χ_q/T^2	0.882(10)	0.895(16)	0.890(14)	0.895(8)	0.897(3)
$G_V^{(2)}/(\tilde{\chi}_q G_V^{(2),free})$	1.273(4)	1.214(2)	1.207(1)	1.193(1)	1.189(13)
$G_V(1/2)/(\tilde{\chi}_q G_V^{free}(1/2))$	1.276(14)	1.234(10)	1.226(10)	1.216(8)	1.211(9)
$G_V(1/4)/(\tilde{\chi}_q G_V^{free}(1/4))$	1.333(9)	1.235(6)	1.213(4)	1.202(5)	1.190(7)
$G_{ii}(1/2)/(\tilde{\chi}_q G_{ii}^{free}(1/2))$	1.184(7)	1.156(6)	1.152(5)	1.145(6)	1.142(9)
$G_{ii}(1/4)/(\tilde{\chi}_q G_{ii}^{free}(1/4))$	1.302(7)	1.213(6)	1.193(3)	1.183(5)	1.172(7)

TABLE IV. Quark number susceptibility (χ_q/T^2), the curvature of the vector correlation function at the mid-point ($G_V^{(2)}$) and several values of the vector correlation functions expressed in units of the corresponding free field values and normalized with the quark number susceptibility. Results are from calculations on lattices of size $128^3 \times N_\tau$. The last column gives the continuum extrapolated results. The quark number susceptibility has been renormalized using the renormalization constants listed in Table I. In all other ratios renormalization constants drop out.

value, $R_V^{(2,0)} < R_{V,free}^{(2,0)}$. The spatial part alone, $G_{ii}(\tau T)/G_{ii}^{free}(\tau T)$, on the other hand drops when approaching $\tau T = 1/2$ (see Fig. 3). This suggests $R_{ii}^{(2,0)} > R_{ii,free}^{(2,0)}$.

Also in calculations of the time-time component of the vector correlation function we find that finite volume, as well as cut-off effects, are small. In Fig. 2 we show results for $-G_{00}(\tau T)/T^3$ for all lattice sizes analyzed by us. The left hand part of Fig. 2 shows results obtained on lattices with different spatial extent at fixed lattice cut-off. Except for the smallest aspect ratio, $N_\sigma/N_\tau = 2$, the results agree within statistical errors of about 1%. The right hand part shows results obtained on our largest spatial lattice, $N_\sigma = 128$, at four different values of the lattice cut-off. This shows that also cut-off effects are small in the calculation of the time-time component of the vector correlation function, *i.e.* the quark number susceptibility. Apparently the fact that we use a non-conserved local current does not significantly alter the spectral properties of the time-time correlator. Except for short distances it is to a good degree τ -independent. We summarize results for $\chi_q/T^2 \equiv -G_{00}(\tau T)/T^3$ calculated on the $128^3 \times N_\tau$ lattices in Table IV.

We note that at $T \simeq 1.45T_c$ the quark number susceptibility, χ_q/T^2 , is about 10% smaller than the free field value $\chi_q^{free}/T^2 = 1$ which is in accordance with calculations performed with staggered fermions.

In Fig. 3 we show separately results for the space-space component of the vector current correlation function, $G_{ii}(\tau T)/T^3$, and the combined vector correlator, $G_V(\tau T)/T^3$. In both cases we normalized the correlation function to the corresponding free correlator, $G_H^{free}(\tau T)/T^3$. Of course, ratios for $H = V$ and $H = ii$ are related through Eq. II.8 and provide identical information on the vector spectral function representing these correlators.

It is apparent that the short distance part of the vector correlation functions is strongly influenced by finite cut-off effects. To some extent one can eliminate cut-off effects by calculating the free field correlation functions on lattices with finite temporal extent and considering the ratio $G_V/G_V^{free,lat}$ rather than the ratio obtained by normalizing with the free vector correlator in the continuum limit. A comparison between the lower and upper panels of Fig. 3 indeed shows a reduction of cut-off effects, although the short distance part $\tau T \lesssim 0.2$ still deviates substantially from the free field values. However, in the entire Euclidean time interval, where cut-off effects are under control and a continuum extrapolation is possible for $\tau T \in [0.2 : 0.5]$, $G_V(\tau T)$ as well as $G_{ii}(\tau T)$ stay close to the corresponding free field correlation functions. We also note that in the continuum limit the ratios shown in Fig. 3 will all approach the same value in the limit $\tau T \rightarrow 0$ as all correlation functions diverge for $\tau T \rightarrow 0$ and the fact that G_V and G_{ii} differ by a constant becomes unimportant. Moreover, note that the data shown in this figure have been divided by the quark number susceptibility, χ_q/T^2 , to avoid the usage of any renormalization constants. Multiplying the data shown in Fig. 3 by the quark number susceptibility given in Table IV gives the ratio of the vector correlation functions and the free vector correlator. These values are about 10% smaller than the data shown in Fig. 3. We therefore expect that in the continuum limit deviations of the vector correlation function as well as its spatial component from the corresponding free correlator remain smaller than 9% for all $\tau T \geq 0.2$.

B. Continuum extrapolation of the vector correlation function

For three values of Euclidean time, $\tau T = 1/4, 3/8, 1/2$, we have numerical results from calculations at all four values of the lattice cut-off. In these cases we performed directly a continuum extrapolation of the correlation functions using data from simulations on lattices with temporal extent $N_\tau = 24, 32$ and 48. Specifically, we extrapolated the ratio of correlation functions $G_H(\tau T)/(\tilde{\chi}_q G_V^{free}(\tau T))$ by using a quadratic ansatz in $aT = 1/N_\tau$. At other values of τT we use spline interpolations of the data sets on the $N_\tau = 24$ and 32 lattices to perform continuum extrapolations at Euclidean time distances available on the $N_\tau = 48$ lattices, *i.e.* $\tau T = k/48$ for $9 \leq k \leq 24$. Continuum extrapolations at a few selected Euclidean time separations are shown in Fig. 4. We find that results obtained from the continuum extrapolation of correlators normalized with the free lattice and continuum correlation functions, respectively, agree within errors. The resulting continuum extrapolation of the vector correlation function obtained in this way is shown in Fig. 5. Data for $\tau T = 1/4$ and $1/2$ are also summarized in Table IV.

From Fig. 5 we conclude that the largest deviation of $G_V(\tau T)$ from the free vector correlation

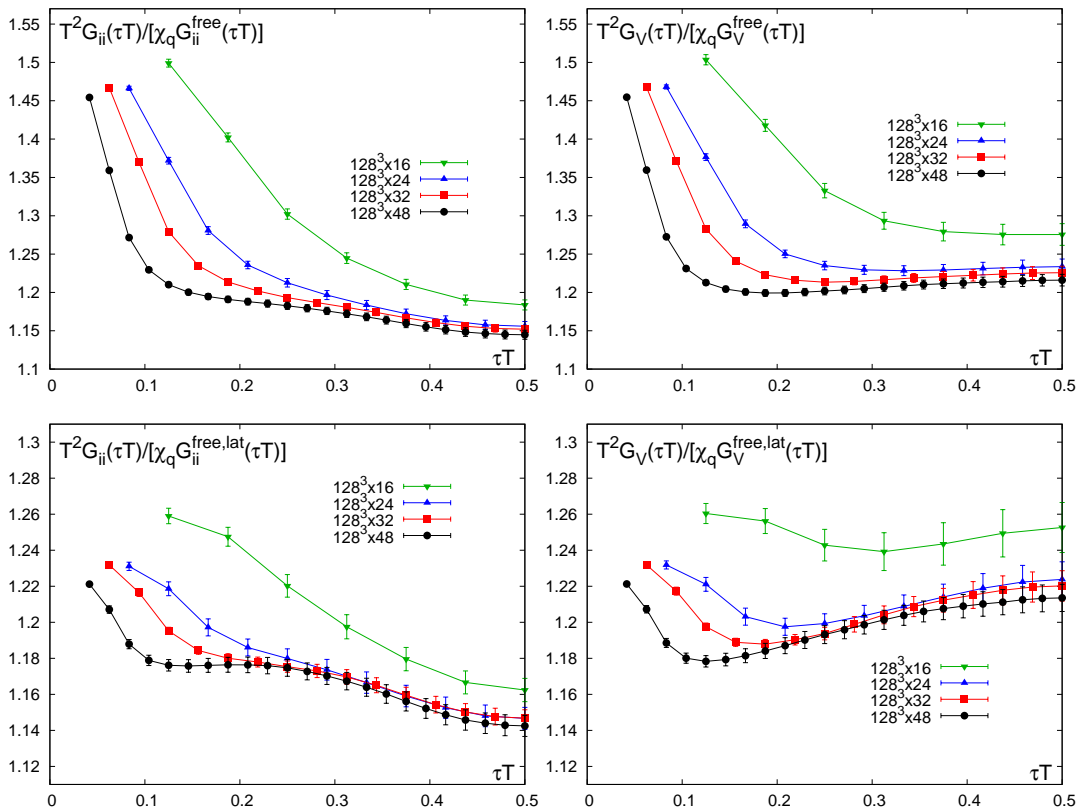


FIG. 3. The space-space component of the vector correlation function, $G_{ii}(\tau T)/T^3$, calculated at $T \simeq 1.45T_c$ on lattices of size $128^3 \times N_\tau$ versus Euclidean time τT (left) and the total vector correlator $G_V(\tau T)/T^3$ (right). Both correlators have been normalized by the continuum version of the corresponding free vector correlation function defined in Eq. III.3 (upper part) and the discretized version of the free vector correlation function calculated on infinite spatial volumes with fixed N_τ (lower part), respectively.

function occurs at $\tau T = 1/2$. Taking into account the normalization with $\tilde{\chi}_q$ we obtain from Table IV

$$\begin{aligned} \frac{G_V(1/2)}{G_V^{free}(1/2)} &= 1.086 \pm 0.008, \\ \frac{G_V(1/4)}{G_V^{free}(1/4)} &= (0.982 \pm 0.005) \frac{G_V(1/2)}{G_V^{free}(1/2)} \end{aligned} \quad (\text{IV.2})$$

where the second relation has been obtained from a jackknife analysis of the ratio $G_V(1/4)/G_V(1/2)$.

We note that the increase of $G_V(\tau T)/G_V^{free}(\tau T)$ with τT is significant. It becomes apparent only for sufficiently small lattice spacing, *i.e.* for large N_τ , in particular in the normalization with the free continuum vector correlator. The rise with τT is a direct indicator that the vector spectral function in the low- ω region is different from the free case, and is part of the motivation for the fit ansätze discussed in Section V.

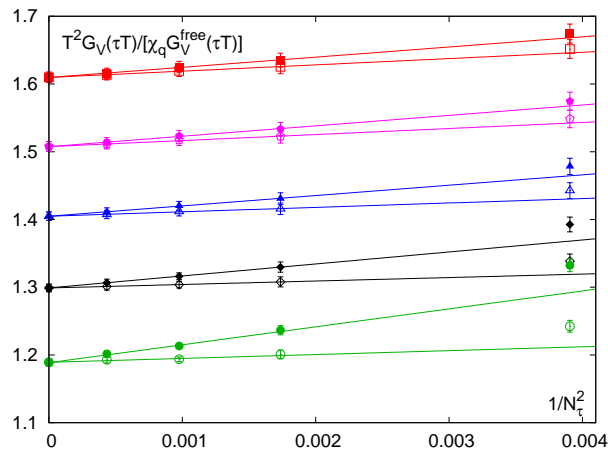


FIG. 4. The ratio of the vector correlation function, $G_V(\tau, T)$, normalized with the quark number susceptibility and the free vector correlation function calculated in the continuum (full symbols) and on lattices with temporal extent N_τ (open symbols). Shown are results for five values of Euclidean time, $\tau T = 0.1875, 0.25, 0.3125, 0.375$ and 0.5 (bottom to top), on lattices with temporal extent $N_\tau = 16, 24, 32$ and 48 . For distances larger than $\tau T = 0.1875$ data have been shifted in steps of 0.1 for better visibility. For $\tau T = 0.1875$, and 0.3125 spline interpolations have been used on the $N_\tau = 24$ lattice to estimate results at these Euclidean time separations. Note that the far most right data set, corresponding to $N_\tau = 16$, has not been included in the extrapolation.

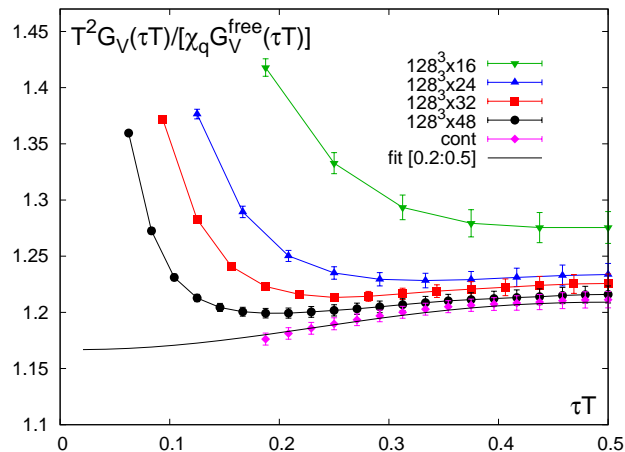


FIG. 5. Continuum extrapolation of the vector correlation function.

C. Curvature of the vector current correlation function

Here we want to discuss the calculation of the second and fourth thermal moment of the vector spectral function defined in Eq. III.1. From Eq. III.5 we expect that the second thermal moment will be closer to the free field value than the correlation function at the mid-point itself.

We analyze the ratio of the mid-point subtracted correlation function, $\Delta_V(\tau T)$, introduced in Eq. III.6. Results for $\Delta_V(\tau T)$ calculated at the four different values of the lattice-cut-off are shown

in Fig. 6. Again we perform spline interpolations of results obtained on lattices with temporal extent $N_\tau = 24$ and 32 . These interpolated data together with the results obtained on the $N_\tau = 48$ lattices are then extrapolated to the continuum limit taking into account corrections of $\mathcal{O}((aT)^2)$. The extrapolated data at distances $k/48$ are shown also in Fig. 6. These extrapolated data have been fitted to a quartic polynomial as indicated by the Taylor expansion given in Eq. III.6. From this fit we obtain

$$\frac{G_V^{(2)}}{G_V^{(2),free}} = 1.067 \pm 0.012 \quad . \quad (\text{IV.3})$$

Fits of the vector correlation function and the mid-point subtracted correlator are, of course, correlated. We made use of this and also calculated the ratio of the second thermal moment and the correlation function at the mid-point on jackknife blocks . We find

$$\begin{aligned} \frac{G_V^{(2)}}{G_V^{(0)}} &= (0.982 \pm 0.012) \frac{G_V^{(2),free}}{G_V^{(0),free}} \quad , \\ \frac{G_{ii}^{(2)}}{G_{ii}^{(0)}} &= (1.043 \pm 0.010) \frac{G_{ii}^{(2),free}}{G_{ii}^{(0),free}} \quad . \end{aligned} \quad (\text{IV.4})$$

Although the statistical significance of the deviation of $G_V^{(2)}/G_V^{(0)}$ from the free case is marginal, the difference is consistent with the behavior of $G(\tau T)/G^{free}(\tau T)$ close to $\tau T = 1/2$ shown in Fig. 5. At large enough τT the latter has a positive slope in τT , which approaches zero from above when τT reaches $1/2$, and a small negative curvature that is in the limit of τT going to $1/2$ proportional to $R_V^{(2,0)} - R_{V,free}^{(2,0)}$, as shown in Eq. III.5.

We will show in the following that this puts stringent bounds on the magnitude of any contribution to the vector correlation function that may arise from a peak in the vector spectral function at small energies. We also tried to look at the fourth thermal moment, which could be obtained from the curvature of the fits shown in Fig. 6. However, at present our numerical results do not allow to draw a firm conclusion about its value.

V. ANALYSIS OF THE VECTOR CURRENT CORRELATION FUNCTION

In the previous section we have presented results for the vector current correlation function in quenched QCD at $T \simeq 1.45T_c$. For Euclidean times $\tau T \in [0.2, 0.5]$ the results could be safely extrapolated to the continuum limit. As the correlation functions $G_V(\tau T)$ and $G_{ii}(\tau T)$ are closely related to each other, we now concentrate on a discussion of the latter. Let us summarize our basic findings for the $G_{ii}(\tau T)$:

- (i) The correlation function at $\tau T = 1/2$ is about 2% larger than the corresponding free field value, $G_{ii}(1/2)/G_{ii}^{free}(1/2) = 1.024(8)$
- (ii) The deviation from the free field value increases with decreasing Euclidean time. At $\tau T = 1/4$ the ratio is $G_{ii}(1/4)/G_{ii}^{free}(1/4) = 1.051(7)$
- (iii) The second moment of the vector spectral function deviates from the free field value by about 7%, $G_V^{(2)}/G_V^{(2),free} = G_{ii}^{(2)}/G_{ii}^{(2),free} = 1.067(12)$

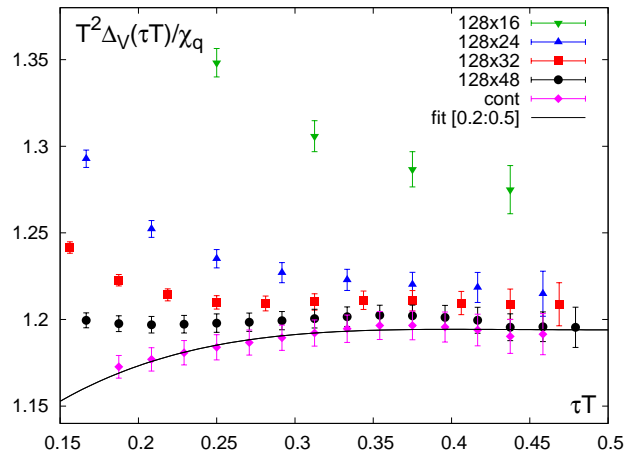


FIG. 6. The mid-point subtracted vector correlation function normalized to the corresponding difference for the free vector correlation function. Shown is the ratio as defined in Eq. III.6 but normalized by the quark number susceptibility. The continuum extrapolation is discussed in the text.

This suggests that the spectral function of the free theory is a good starting point for the description of the vector correlator. We will use the knowledge about the asymptotic behavior of the vector spectral function at low and high energies, presented in Section II, to construct ansätze for the spectral function at high temperature. This is done in two steps. In the next subsection we discuss a straightforward implementation of the low and high energy constraints by using a combination of the free continuum spectral function and a Breit-Wigner contribution. Subsequently we will generalize this ansatz and discuss a class of spectral functions for which the continuum contribution is cut off at some low energy value and present also results from a MEM analysis. We find that the most straightforward approach already gives an excellent description of all our data.

A. Breit-Wigner + continuum ansatz

We start with the analysis of our results for the vector correlation function by using the ansatz,

$$\rho_{00}(\omega) = -2\pi\chi_q\omega\delta(\omega) , \quad (\text{V.1})$$

$$\rho_{ii}(\omega) = 2\chi_q c_{BW} \frac{\omega\Gamma/2}{\omega^2 + (\Gamma/2)^2} + \frac{3}{2\pi} (1+k) \omega^2 \tanh(\omega/4T) . \quad (\text{V.2})$$

This ansatz depends on four temperature dependent parameters; the quark number susceptibility $\chi_q(T)$, the strength ($c_{BW}(T)$) and width ($\Gamma(T)$) of the Breit-Wigner peak and the parameter $k(T)$ that parametrizes deviations from a free spectral function at large energies. At high temperature and for large energies, $\omega/T \gg 1$, we expect to find $k(T) \simeq \alpha_s/\pi$. Note that $k(T)$ will also depend on ω and actually will vanish for $\omega \rightarrow \infty$ at fixed T . We will treat here $k(T)$ as a constant and will not take into account any running of α_s . As will become clear in the following, already this minimal ansatz provides a good description of current numerical results for the vector correlation functions $G_{ii}(\tau T)$ and $G_{00}(\tau T)$. In fact, it is quite straightforward to use the latter for a determination of

$\chi_q(T)$.

The parameters of the Breit-Wigner term can be extracted from fits to the vector correlation function. As pointed out in Eq. II.8 the correlation functions G_V and G_{ii} agree up to an additive constant, the quark number susceptibility. It thus suffices to analyze one of them.

With the ansatz for the spectral function given in Eq. V.2 and $\tilde{\Gamma} = \Gamma/T$ we obtain

$$\tilde{G}_{ii}(\tau T) = (1 + k(T)) \tilde{G}_V^{free}(\tau T) + c_{BW} \tilde{\chi}_q F_{BW}(\tau T, \tilde{\Gamma}), \quad (\text{V.3})$$

with

$$F_{BW}(\tau T, \tilde{\Gamma}) = \frac{\tilde{\Gamma}}{2\pi} \int_0^\infty d\tilde{\omega} \frac{\tilde{\omega}}{(\tilde{\Gamma}/2)^2 + \tilde{\omega}^2} \frac{\cosh(\tilde{\omega}(\tau T - 1/2))}{\sinh(\tilde{\omega}/2)}. \quad (\text{V.4})$$

With this normalization one has $\lim_{\tilde{\Gamma} \rightarrow 0} F_{BW}(\tau T, \tilde{\Gamma}) = 1$ and $\lim_{\tilde{\Gamma} \rightarrow \infty} F_{BW}(\tau T, \tilde{\Gamma}) = 0$.

Note that with this ansatz the dependence on the continuum contribution and thus the dependence on $k(T)$ can easily be eliminated by taking appropriately weighted differences of $G_{ii}(\tau T)$ at two values of Euclidean time. Similarly we obtain for the mid-point subtracted correlation functions, introduced in Eq. III.6,

$$\Delta_V(\tau T) = 1 + k(T) + c_{BW} \tilde{\chi}_q \frac{F_{BW}(\tau T, \tilde{\Gamma}) - F_{BW}(1/2, \tilde{\Gamma})}{\tilde{G}_V^{free}(\tau T) - \tilde{G}_V^{free}(1/2)}. \quad (\text{V.5})$$

At $\tau T = 1/2$ this fit ansatz yields results for the zeroth and second moment of the spectral function as introduced in Eq. III.5 and Eq. III.6,

$$\begin{aligned} \tilde{G}_{ii}(1/2) &= 2(1 + k(T)) + c_{BW} \tilde{\chi}_q F_{BW}^{(0)}(\tilde{\Gamma}), \\ \Delta_V(1/2) &= 1 + k(T) + c_{BW} \tilde{\chi}_q \frac{F_{BW}^{(2)}(\tilde{\Gamma})}{\tilde{G}_V^{(2),free}}, \end{aligned} \quad (\text{V.6})$$

with

$$F_{BW}^{(2n)}(\tilde{\Gamma}) = \frac{1}{(2n)!} \frac{\tilde{\Gamma}}{2\pi} \int_0^\infty d\tilde{\omega} \frac{\tilde{\omega}^{2n+1}}{\left((\tilde{\Gamma}/2)^2 + \tilde{\omega}^2\right) \sinh(\tilde{\omega}/2)}. \quad (\text{V.7})$$

In the limit $\tilde{\Gamma} \rightarrow 0$ the thermal moments $F_{BW}^{(2n)}$ vanish for all $n > 0$ and the fit ansatz for $\Delta_V(\tau T)$ becomes a constant which relates to the deviations of the vector correlation function from the free field correlator at short distances. For all $\tilde{\Gamma} > 0$, however, the right hand side of Eq. V.5 is a monotonically increasing function of τT . We note that even for our largest lattice this feature is not yet obvious from the data. However, it becomes apparent in the continuum extrapolation of the mid-point subtracted correlation function. Having established the monotonic rise of $\Delta_V(\tau T)$ is important for motivating our fit ansatz.

Fitting the continuum extrapolated correlation function $G_{ii}(\tau T)$ in the interval $[0.2 : 0.5]$ together with the second thermal moment $G_V^{(2)}$ to constrain the fit, we obtain

$$k = 0.0465(30), \quad \tilde{\Gamma} = 2.235(75), \quad 2c_{BW} \tilde{\chi}_q / \tilde{\Gamma} = 1.098(27). \quad (\text{V.8})$$

This three parameter fit has a $\chi^2/d.o.f. = 0.06$ for 12 degrees of freedom. The small $\chi^2/d.o.f.$ clearly reflects that even after the continuum extrapolation data at different distances are strongly

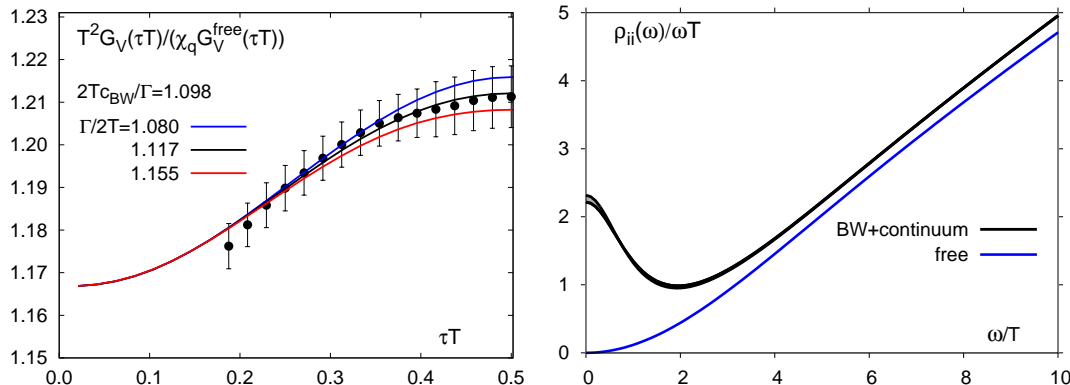


FIG. 7. Data for the continuum extrapolation of $T^2 G_V(\tau T)/(\chi_q G_V^{free}(\tau T))$ and the fit result for fixed $c_{BW}/\tilde{\Gamma}$ and $k(T)$ (left). The three curves show the result from a fit in the interval $\tau T \in [0.2 : 0.5]$ (central) and results obtained by varying $\tilde{\Gamma}$ within its error band. In the right hand figure we show the spectral function obtained from the fit and compare with the free spectral function.

correlated. Nonetheless, the fit provides an excellent description of the data. To illustrate the sensitivity of our fit to the low energy Breit-Wigner contribution and its dependence on Euclidean time, we show the fit to the data for $G_V(\tau T)$ normalized to the free vector correlation function and the quark number susceptibility in Fig. 7. The error band shown in this figure corresponds to the width of the Breit-Wigner peak. The spectral function obtained from this fit is shown in the right hand part of the figure. Here also the error band arising from a variation of the width Γ is shown.

It is clear from Fig. 7, that the vector correlation function is sensitive to the low energy, Breit-Wigner contribution only for distances $\tau T \gtrsim 0.25$. Taking into account also the value of the second thermal moment, the fits to the large distance regime return fit parameters which are well constrained. As a consequence we obtain a significant result for the electrical conductivity, which is directly proportional to the fit parameter $c_{BW}/\tilde{\Gamma}$,

$$\frac{\sigma}{T} = \frac{C_{em}}{6} \lim_{\omega \rightarrow 0} \frac{\rho_{ii}(\omega)}{\omega T} = \frac{2C_{em}}{3} \frac{c_{BW}\tilde{\chi}_q}{\tilde{\Gamma}} = (0.37 \pm 0.01)C_{em}, \quad (\text{V.9})$$

which (accidentally) is close to the result found in [20] using staggered fermions with unrenormalized currents. It is more than an order of magnitude larger than the electrical conductivity in a pion gas [40].

It should be obvious that this determination of the electrical conductivity is sensitive to the ansatz made for the spectral function in our analysis of the correlation functions. With this simple ansatz we obtain good fits of the vector correlation function with a very small chi-square per degree of freedom. However other ansätze may provide an equally good description of the current set of data. We will explore this in the next subsection by generalizing the current ansatz.

We also note that the value determined for the correction to the free field behavior at large energies $k \simeq 0.05$ at $T \simeq 1.45T_c$ is quite reasonable. Using the relation to the perturbative result, $k = \alpha_s/\pi$ yields for the temperature dependent running coupling $g^2(T) = 4\pi\alpha_s \simeq 2$ which is in good agreement with other determinations of temperature dependent running couplings at high

energies or short distances [38].

B. Breit-Wigner plus truncated continuum ansatz

In the ansatz used in the previous subsection the continuum part, *i.e.* a contribution proportional to the free spectral function, contributes to $\rho_{ii}(\omega)$ for all ω . Also in the highly non-perturbative low momentum region there thus is a contribution proportional to ω^3/T arising from the continuum part. In order to analyze its influence on the low energy structure of the spectral function we smoothly truncate the continuum contribution at some energy ω_0 . We thus replace the spectral part of our fit ansatz by

$$\begin{aligned} \rho_{ii}(\omega) &= 2\chi_q c_{BW} \frac{\omega\Gamma/2}{\omega^2 + (\Gamma/2)^2} + \frac{3}{2\pi} (1+k) \omega^2 \tanh(\omega/4T) \Theta(\omega_0, \Delta_\omega) \\ \Theta(\omega_0, \Delta_\omega) &= \left(1 + e^{(\omega_0^2 - \omega^2)/\omega\Delta_\omega}\right)^{-1}. \end{aligned} \quad (\text{V.10})$$

In the limit $\Delta_\omega \rightarrow 0$ the function $\Theta(\omega_0, \Delta_\omega)$ becomes a Θ -function with discontinuity at ω_0 . We also used other cut-off functions for the continuum contribution, which lead to similar conclusions. We prefer the above version as it insures that the continuum contribution vanishes exponentially at $\omega = 0$. This allows, for instance, to replace the simple free field ansatz, used for the continuum in Eq. V.10, by the HTL or further improved spectral functions, which have power-law divergences at small ω .

As discussed in the previous section we perform three parameter fits with c_{BW} , Γ and k as free parameters for several values of ω_0 and Δ_ω . We find that fits become worse with increasing ω_0 and/or increasing Δ_ω . In both cases eventually too much of the continuum part at high energies gets suppressed. For small values of ω_0 and Δ_ω the Breit-Wigner term compensates for the continuum contribution that has been cut off by increasing the low energy contribution, *i.e.* the intercept at $\omega = 0$ (electrical conductivity) rises. Results from fits which all lead to $\chi^2/d.o.f.$ smaller than unity are shown in Fig. 8. As ω_0 and Δ_ω increase the $\chi^2/d.o.f.$ of the fits shown in this figure rises from its minimal value of about 0.06, obtained for $\omega_0/T = \Delta_\omega/T = 0$, to unity. All fit parameters corresponding to the curves shown in Fig. 8 are summarized in Table V

In particular the second moment of the correlation function normalized by the correlation function at the mid-point, *i.e.* the ratio $R_{ii}^{(2,0)}$ introduced in Eq. III.5, reacts quite sensitive to the truncation of the continuum part of the spectral function. This is shown in Fig. 9, where we compare the ratio $R_{ii}^{(2,0)}$ extracted from our continuum extrapolated data (error band) with fit results obtained for different values of ω_0 . The dependence on Δ_ω , on the other hand, is less pronounced.

We conclude from this analysis that for $\omega/T \gtrsim (2-4)$ acceptable spectral functions should not deviate significantly from the perturbative or free field like behavior. Moreover, the structure of the spectral function in the energy range $\omega/T \lesssim 2$ is sensitive to the form of the fit ansatz. Within the class of functions analyzed here the fits do, however, favor a small value for the cut-off ω_0 and a small value for the intercept of $\rho_{ii}(\omega)/\omega$ at $\omega = 0$.

These findings are consistent with the default model dependence of a MEM analysis which we will briefly discuss in the next subsection.

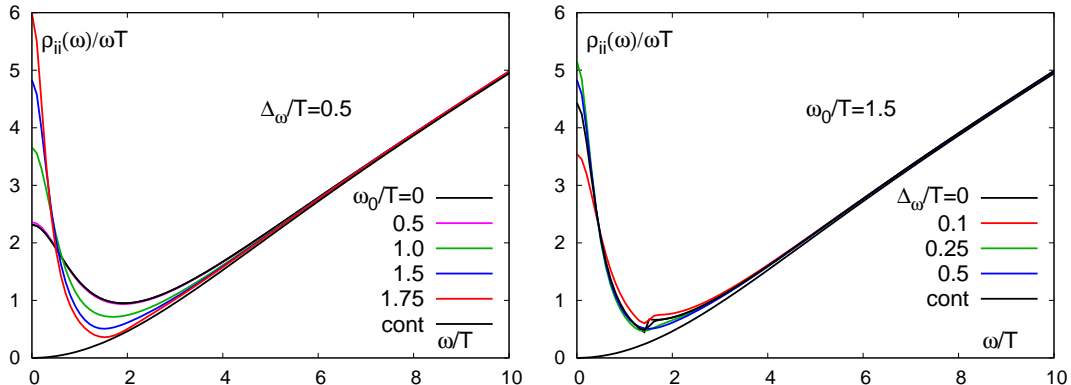


FIG. 8. Spectral functions obtained from fits to the vector correlation function using the ansatz given in Eq. V.10. For comparison we also show only the continuum part of the spectral function. The left hand figure shows results for different values of the cut-off (ω_0) and fixed width (Δ_ω). The right hand figure shows results for fixed $\omega_0/T = 1.5$ and several values of Δ_ω . The curve labeled 'cont' is the continuum contribution to the fit described in Eq. V.3.

ω_0/T	Δ_ω/T	$2c_{BW} \tilde{\chi}_q/\tilde{\Gamma}$	$\tilde{\Gamma}$	k	χ^2/dof
0.0	0.5	1.290(46)	2.091(112)	0.1677(42)	0.08
0.5	0.5	1.315(43)	2.038(114)	0.1683(41)	0.11
1.0	0.5	2.039(22)	1.198(25)	0.1739(4)	0.19
1.5	0.5	2.694(19)	0.866(15)	0.1760(4)	0.56
1.75	0.5	3.338(18)	0.679(15)	0.1774(4)	1.00
1.5	0.0	2.471(20)	0.947(17)	0.1778(4)	0.32
1.5	0.1	1.976(23)	1.232(27)	0.1741(4)	0.36
1.5	0.25	2.873(19)	0.808(13)	0.1773(4)	0.39
1.5	0.5	2.694(19)	0.866(15)	0.1760(4)	0.56

TABLE V. Parameters for the fits shown in Fig. 8 left (upper part) and right (lower part). The last column gives the χ^2/dof of these fits.

C. Analysis of vector correlation functions using the Maximum Entropy Method

So far we did not make use of the Maximum Entropy Method that has been used in most other lattice studies of the spectral function in the vector channel. Here we want to discuss to what extent the analysis presented in the previous subsections can be reproduced in a MEM analysis, or whether a MEM analysis may improve over the result obtained with an ansatz for the spectral function. We performed a MEM analysis of the renormalized vector correlation function on our finest lattice using the modified kernel which has been introduced in [20] and further refined in [41].

To start the MEM analysis of a given meson correlation function we need to specify a default model that incorporates all prior knowledge about the spectral function we want to determine. Before presenting the analysis based on default models related to the fits discussed in the previous subsections we performed a MEM analysis in analogy to what we had done earlier [18]. We used as

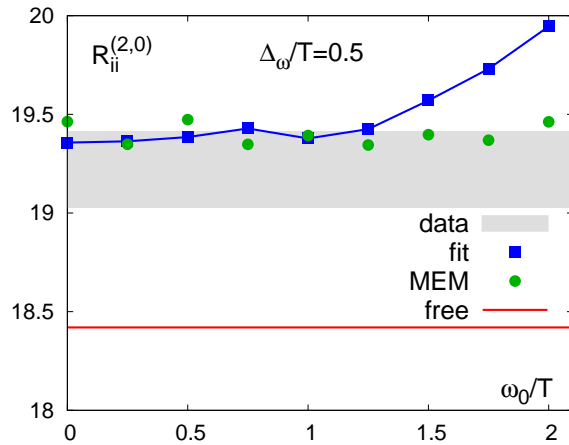


FIG. 9. The ratio of second and zeroth thermal moment of the correlation function $G_{ii}(\tau T)$ obtained from fits with different values for the continuum cut-off parameter ω_0/T and fixed Δ_ω . Circles show results of a MEM analysis where the fits have been used as default model. The band gives the result extracted from the continuum extrapolated correlation function. The lower curve shows the corresponding free field (infinite temperature) value, which is about 5% smaller than the value obtained at $T \simeq 1.45T_c$.

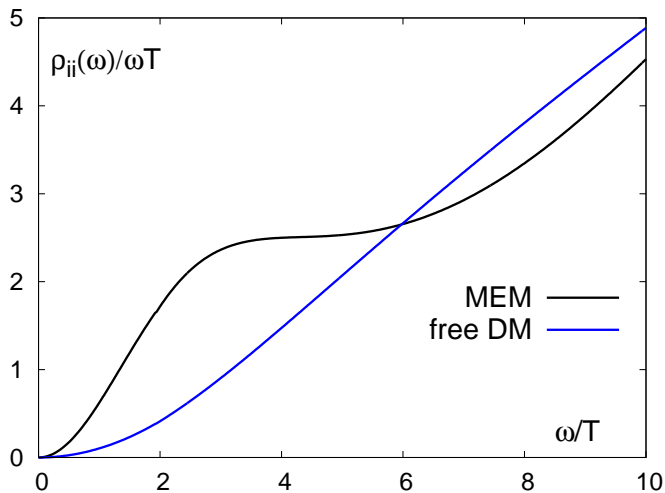


FIG. 10. Spectral functions obtained from a maximum entropy analysis using the free spectral function as default model.

default model the free spectral function, *i.e.* an ansatz that does not include a contribution linear in ω at small energies but rather $\rho_{ii}^{DM}(\omega)/\omega \sim \omega^2/T$. This default model together with the resulting output spectral function is shown in Fig. 10. Apparently this ansatz also forces $\rho^{mem}(\omega)/\omega$ to vanish at $\omega = 0$. In particular, it leads to a suppression of the dilepton rate at small energies. The small contribution at small energies is compensated by large contributions at $\omega \sim (2 - 4)T$. This feature has been observed also in our first analysis of vector spectral functions [18].

To allow a MEM analysis to find a contribution $\rho(\omega) \sim \omega$ at the origin this possibility needs to

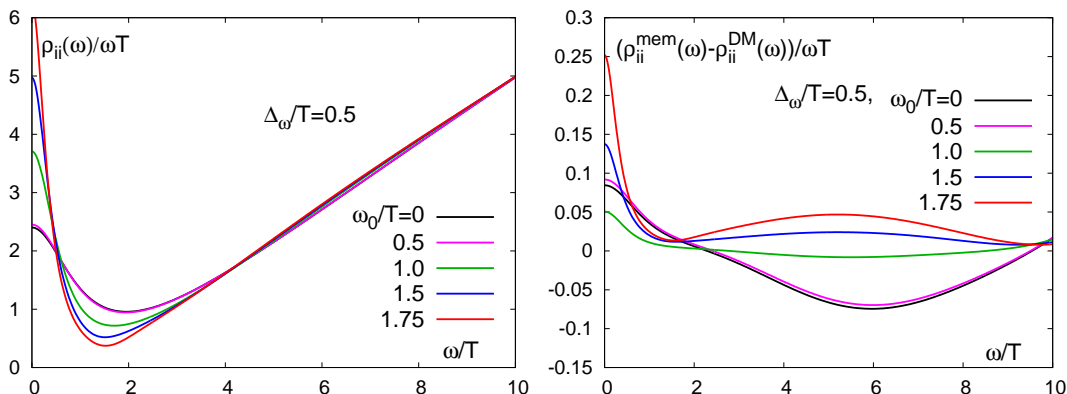


FIG. 11. Spectral functions obtained from a maximum entropy analysis using for the default model the spectral functions shown in Fig. 8(left). The right hand figure shows the difference between the output spectral function obtained from the MEM analysis and the input spectral function used in each case.

be offered by the default model^c It thus seems to be appropriate to use the result of the analysis presented in the previous subsections as default model in a MEM analysis. It definitely summarizes the best knowledge we have at present about the spectral function in the vector channel. Using the un-modified version of the Breit-Wigner plus continuum ansatz, Eq. V.2, as default model changes results only little and leads to an output spectral function that is compatible with the input form. It also reproduces the result obtained for the electrical conductivity given in Eq. V.9.

In order to judge the stability of the spectral function obtained with our fit ansatz, we used a class of default models of the form given in Eq. V.10. We performed a MEM analysis using as input default models the spectral functions shown in Fig. 8. We controlled the error on the output spectral functions by performing the MEM analysis on jackknife blocks. In this way we find that the error of the output spectral functions never is larger than 10% for small energies and is below 5% for $\omega/T \gtrsim 8$. In Fig. 11(left) we show results for spectral functions obtained in a MEM analysis by using a set of default models with varying ω_0 and fixed Δ_ω . The right hand figure shows the difference between the input default models and the output spectral functions. We note that these differences correspond to changes in the spectral functions which are generally smaller than 5%. They increase in particular for small values of ω as the $\chi^2/d.o.f.$ of the input default model gets worse. We also note that the MEM analysis reproduces the calculated ratio of thermal moments as well or even better than the fits used as a default model, although the value of the thermal moments itself did not directly enter the MEM analysis.

VI. ELECTRICAL CONDUCTIVITY, THERMAL DILEPTON AND PHOTON RATES

Here we want to discuss the consequences of our results for thermal dilepton rates as well as the electrical conductivity and the related soft photon rate.

^c On the other hand, in correlation functions for quantum number channels where no transport contribution is present, MEM is flexible enough to suppress or eliminate completely a contribution $\rho(\lambda) \sim \lambda$ included in the default model. This is, for instance, the case in the pseudo-scalar channel.

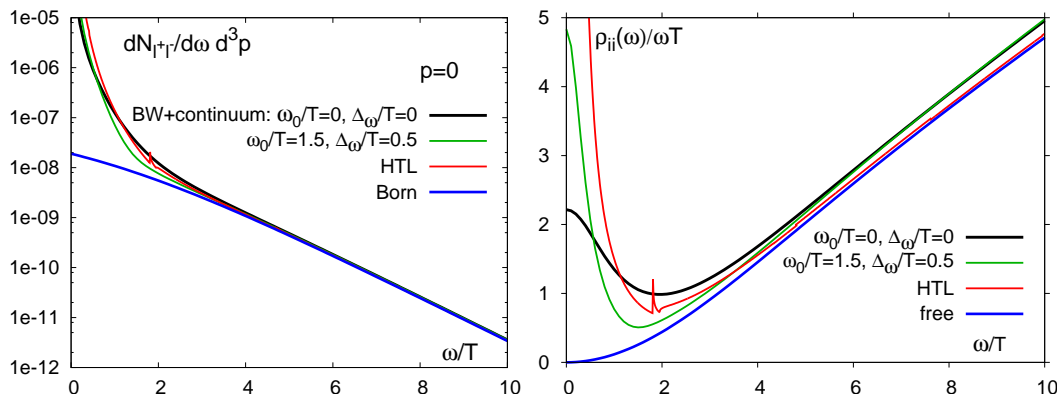


FIG. 12. Thermal dilepton rate in 2-flavor QCD (left). Shown are results from fits without a cut-off on the continuum contribution ($\omega_0/T = 0$) and with the largest cut-off tolerable in our fit ansatz ($\omega_0/T = 1.5$). The HTL curve is for a thermal quark mass $m_T/T = 1$ and the Born rate is obtained by using the free spectral function. The right hand part of the figure shows the spectral functions that entered the calculation of the dilepton rate.

In Fig. 12 we show the thermal dilepton rate calculated from Eq. II.14 for two massless (u, d) flavors. We use the results obtained with our Breit-Wigner plus continuum fit ansatz, Eq. V.2, as well as results obtained with a truncated continuum term. For the latter we use the case, $\omega_0/T = 1.5$, $\Delta_\omega/T = 0.5$, which gave a $\chi^2/d.o.f$ of about 1. These results are compared to a dilepton spectrum calculated within the hard thermal loop approximation [12] using a thermal quark mass $m_T/T = 1$. Obviously the results are in good agreement for all $\omega/T \gtrsim 2$. For $1 \lesssim \omega/T \lesssim 2$ differences between the HTL spectral function and our numerical results is about a factor two, which also is the intrinsic uncertainty in our spectral analysis. At energies $\omega/T \lesssim 1$ the HTL results grow too rapidly, as is well known.

In the limit $\omega \rightarrow 0$ the results for $\rho_{ii}(\omega)/\omega$, and thus also for the electrical conductivity, are sensitive to the choice of fit ansatz. Within the class of ansätze used by us a small value of $\rho_{ii}(\omega)/\omega$ seems to be favored. Our current analysis suggests,

$$2 \lesssim \lim_{\omega \rightarrow 0} \frac{\rho_{ii}(\omega)}{\omega T} \lesssim 6 \quad \text{at } T \simeq 1.45 T_c. \quad (\text{VI.1})$$

This translates into an estimate for the electrical conductivity

$$1/3 \lesssim \frac{1}{C_{em}} \frac{\sigma}{T} \lesssim 1 \quad \text{at } T \simeq 1.45 T_c. \quad (\text{VI.2})$$

Using Eq. II.15 this yields for the zero energy limit of the thermal photon rate^d,

$$\lim_{\omega \rightarrow 0} \omega \frac{dR_\gamma}{d^3p} = (0.0004 - 0.0013) T_c^2 \simeq (1 - 3) \cdot 10^{-5} \text{ GeV}^2 \quad \text{at } T \simeq 1.45 T_c. \quad (\text{VI.3})$$

^d Here we used $T_c \simeq 165$ MeV. This is a value relevant for QCD with 2 light quarks rather than the critical temperature for a pure $SU(3)$ gauge theory.

VII. CONCLUSIONS

At a fixed value of the temperature, $T \simeq 1.45T_c$, we have performed a detailed analysis of vector correlation functions in the high temperature phase of quenched QCD. A systematic analysis at different values of the lattice cut-off combined with an analysis of finite volume and quark mass effects allowed us to extract the vector correlation function in the continuum limit for a large interval of Euclidean times, $0.2 \leq \tau T \leq 0.5$. In this interval the correlation function has been determined to better than 1% accuracy. Furthermore, we determined its curvature at the midpoint of the finite temperature Euclidean time interval, $\tau T = 1/2$.

We analyzed the continuum extrapolated vector correlation functions using several fit ansätze that differ in their low momentum structure. We find that the vector correlation function is best fitted by a simple ansatz that is proportional to a free spectral function plus a Breit-Wigner term. Already this simple three parameter ansatz yields a good description of the correlator with a small $\chi^2/d.o.f.$. Other fits with a $\chi^2/d.o.f. \leq 1$ are possible and suggest that the low energy structure of the spectral function currently has a systematic uncertainty of about a factor two. Some generic features of the spectral function are, however, robust. For energies $\omega/T \gtrsim (2-4)$ the spectral function is close to the free form. At present we used an ansatz proportional to the free spectral function to parametrize the spectral function in this regime. However, the hard thermal loop spectral function should give a good description at these energies and can be incorporated in our ansatz, which cuts off the small energy continuum contributions.

For small energies, $\omega/T \lesssim (1-2)$, the spectral function is significantly larger than the free result, but smaller than the HTL spectral function, which diverges at small energies; at energies $\omega/T \simeq 1$ the thermal dilepton rate is about an order of magnitude larger than the leading order Born rate. In order to analyze quantitatively to what extent this enhancement can account for the experimentally observed enhancement of dilepton rates at low energies [9, 42] we will need results on the spectral function at temperatures closer to the transition temperature as well as knowledge on its momentum dependence. With this a complete analysis of dilepton rates that takes into account the hydrodynamic expansion of dense matter created in heavy ion collision will become possible [43].

ACKNOWLEDGMENTS

This work has been supported in part by contracts DE-AC02-98CH10886 with the U.S. Department of Energy, the BMBF under grant 06BI401, the Gesellschaft für Schwerionenforschung under grant BILAER, the Extreme Matter Institute under grant HA216/EMMI and the Deutsche Forschungsgemeinschaft under grant GRK 881. Numerical simulations have been performed on the BlueGene/P at the New York Center for Computational Sciences (NYCCS) which is supported by the U.S. Department of Energy and by the State of New York and the John von Neumann Supercomputing Center (NIC) at FZ-Jülich, Germany.

[1] T. Matsui and H. Satz, Phys. Lett. B **178**, 416 (1986).

- [2] R. Rapp, J. Wambach and H. van Hees, arXiv:0901.3289 [hep-ph]
- [3] J.P. Boon, S. Yip, Molecular Hydrodynamics (McGraw-Hill (1980)).
- [4] D. Forster, Hydrodynamics, Fluctuations, Broken Symmetry, and Correlation Functions, Cambridge, Massachusetts (Perseus-Books (1990)).
- [5] G. Aarts and J. M. Martinez Resco, JHEP **0204**, 053 (2002).
- [6] G. D. Moore and J. M. Robert, arXiv:hep-ph/0607172.
- [7] P. Petreczky and D. Teaney, Phys. Rev. D **73**, 014508 (2006).
- [8] J. Hong and D. Teaney, Phys. Rev. C **82**, 044908 (2010).
- [9] A. Adare et al. (PHENIX Collaboration), Phys. Rev. Lett. **104**, 132301 (2010) and Phys. Rev. C **81**, 034911 (2010).
- [10] for an overview and further references, see for instance: F. Gelis, Nucl. Phys. A **715**, 329 (2003).
- [11] J. P. Blaizot and F. Gelis, Eur. Phys. J. C **43**, 375 (2005).
- [12] E. Braaten and R.D. Pisarski, Nucl. Phys. B **337**, 569 (1990).
- [13] F. Karsch, M. G. Mustafa and M. H. Thoma, Phys. Lett. B **497**, 249 (2001).
- [14] P. B. Arnold, G. D. Moore and L. G. Yaffe, JHEP **0011**, 001 (2000); JHEP **0112**, 009 (2001) and JHEP **0305**, 051 (2003).
- [15] P. Aurenche, F. Gelis, G. D. Moore and H. Zaraket, JHEP **0212**, 006 (2002).
- [16] F. Karsch and H. W. Wyld, Phys. Rev. D **35**, 2518 (1987).
- [17] Y. Nakahara, M. Asakawa and T. Hatsuda, Phys. Rev. D **60** (1999) 091503; M. Asakawa, T. Hatsuda and Y. Nakahara, Prog. Part. Nucl. Phys. **46**, 459 (2001).
- [18] F. Karsch, E. Laermann, P. Petreczky, S. Sticken and I. Wetzorke, Phys. Lett. B **530**, 147 (2002).
- [19] S. Gupta, Phys. Lett. B **597**, 57 (2004).
- [20] G. Aarts, C. Allton, J. Foley, S. Hands and S. Kim, Phys. Rev. Lett. **99**, 022002 (2007).
- [21] J.-P. Blaizot, E. Iancu and A. Rebhan, Phys. Lett. B **523**, 143 (2001).
- [22] R. V. Gavai, S. Gupta and P. Majumdar, Phys. Rev. D **65**, 054506 (2002).
- [23] C. R. Allton *et al.*, Phys. Rev. D **71**, 054508 (2005).
- [24] T. Altherr and P. Aurenche, Z. Phys. C **45**, 99 (1989).
- [25] W. Florkowski and B.L. Friman, Z. Phys. A **347**, 271 (1994).
- [26] K. G. Wilson, Phys. Rev. D **10**, 2445 (1974).
- [27] M. Lüscher, S. Sint, R. Sommer, P. Weisz and U. Wolff, Nucl. Phys. B **491**, 323 (1997).
- [28] M. Lüscher, S. Sint, R. Sommer and H. Wittig, Nucl. Phys. B **491**, 344 (1997).
- [29] C. R. Allton, arXiv:hep-lat/9610016.
- [30] R. G. Edwards, U. M. Heller, T. R. Klassen, Nucl. Phys. **B517**, 377 (1998).
- [31] B. Lucini, M. Teper and U. Wenger, JHEP **0401**, 061 (2004).
- [32] M. Bochicchio, L. Maiani, G. Martinelli, G. C. Rossi and M. Testa, Nucl. Phys. B **262**, 331 (1985).
- [33] M. Guagnelli and R. Sommer, Nucl. Phys. Proc. Suppl. **63**, 886 (1998).
- [34] S. Capitani, M. Luscher, R. Sommer and H. Wittig [ALPHA Collaboration], Nucl. Phys. B **544**, 669 (1999).
- [35] G. M. de Divitiis and R. Petronzio, Phys. Lett. B **419**, 311 (1998).
- [36] M. Guagnelli, R. Petronzio, J. Rolf, S. Sint, R. Sommer and U. Wolff [ALPHA Collaboration], Nucl. Phys. B **595**, 44 (2001).
- [37] K. G. Chetyrkin, J. H. Kuhn and M. Steinhauser, Comput. Phys. Commun. **133**, 43 (2000).
- [38] O. Kaczmarek, F. Karsch, F. Zantow and P. Petreczky, Phys. Rev. D **70**, 074505 (2004); [Erratum-ibid. D **72**, 059903 (2005)].
- [39] G. Aarts and J. M. Martinez Resco, Nucl. Phys. B **726**, 93 (2005).
- [40] D. Fernandez-Fraile and A. Gomez Nicola, Eur. Phys. J. C **62**, 37 (2009); A. G. Nicola and D. Fernandez-Fraile, Nucl. Phys. A **785**, 166 (2007).
- [41] J. Engels and O. Vogt, Nucl. Phys. B **832**, 538 (2010).
- [42] D. Adamova *et al.*, Phys. Lett. B **666**, 425 (2008).
- [43] H. van Hees and R. Rapp, Nucl. Phys. A **806**, 339 (2008).